Catalysis Science & Technology

Accepted Manuscript

ROYAL SOCIETY OF CHEMISTRY

www.rsc.org/catalysis

Lanthanide Ions $Ce^{(III,IV)}$ Substituted for Bi in $BiVO_4$ and Its Enhanced Impact on Visible Light-Driven Photocatalytic Activities

Shaonan Gu, Wenjun Li*, Fangzhi Wang, Hongda Li and Hualei Zhou

Beijing Key Laboratory for Science and Application of Functional Molecular and Crystalline Materials, University of Science and Technology Beijing, Beijing, 100083, China

Abstract: Solid solution photocatalysts $Bi_{1-x}Ce_xVO_{4+\delta}$ ($0 \le x \le 0.3$) were synthesized by Ce substituted for Bi in $BiVO_4$ lattice using a hydrothermal method. X-ray diffraction, Raman spectra and high-resolution transmission electron microscopy revealed that the crystal phase transformed from monoclinic to tetragonal phase, probably due to the substitution of cerium ions in Bi^{3+} positions. UV–vis diffuse reflectance spectroscopy was used to investigate the absorption range and band gap of the photocatalysts. The photocatalytic activities of the prepared samples were examined by studying the degradation of MB and phenol under visible-light irradiation and the best performance was attained for the sample with cerium content of 20 at.% ($Bi_{0.8}Ce_{0.2}VO_{4+\delta}$). The results of photoluminescence spectra and photocurrent demonstrated that the recombination of photogenerated charges was greatly depressed and the photocatalytic activity was improved by the substitution of Ce for Bi in $BiVO_4$. Furthermore, the proposed mechanism of the enhanced photocatalytic activity was discussed.

Key words: Photocatalysis; $BiVO_4$; visible light-driven; lattice defects

Introduction

The application of semiconductor photocatalysts in water cleaning is regarded as an eco-friendly technology to afford organic pollutant degradation using solar energy. In this case, numbers of attempts have been made to pursue the utilization of solar light as efficiently as possible. Bismuth vanadate ($BiVO_4$) has recently become a very attractive material as a promising photocatalyst for organic pollutant because of its worthy photoactivity under visible light.[1,2] As a new type of semiconductor

photocatalyst, $BiVO_4$ possess three main crystalline phase: monoclinic scheelite-type, tetragonal scheelite-type and tetragonal zircon-type.[3,4] Among these phases, monoclinic scheelite-type $BiVO_4$ exhibits higher photocatalytic activity under visible light due to its relatively narrow band gap (*ca.* 2.4 eV), whereas the photocatalytic activity of tetragonal zircon-type $BiVO_4$ is reported to be negligible.[5,6]

The photoactive monoclinic $BiVO_4$ have been obtained through different synthetic methods in the past ten years.[7-10] Nevertheless, low separation efficiency of photogenerated electron–hole pairs is always the main drawback of $BiVO_4$ for its application, which arouses lots of efforts to improve the visible light photocatalytic activity of $BiVO_4$ photocatalysts, including heterojunction structure formation,[11-13] co-catalysts loading[14-16] and impurity doping.[17,18] Particularly, the lanthanide ions with the unique 4*f* electron configuration are regarded as efficient dopants to enhance the photocatalytic activity of $BiVO_4$. To dates, several studies have focused on lanthanide ions modified monoclinic phase $BiVO_4$ photocatalysts, such as Ce,[19] Eu,[20] La, Gd, Nd and Sm.[21] These findings confirmed the enhancement in photocatalytic activities and revealed that the lanthanide ions were present as oxides at the surface of $BiVO_4$. Besides, in a recent paper, Obregón[22] described the enhanced photocatalytic activity of tetragonal zircon-type $BiVO_4$ by Er^{3+} doping. This result showed that the phase of $BiVO_4$ transferred to tetragonal after a small amount of Er^{3+} doped and the photocatalytic performance was improved. And this conclusion was also confirmed by another literature recently.[23] However, the detailed mechanism of the electron–hole pairs separation and the enhanced photocatalytic activity derived from the introduction of lanthanide ions have not been entirely understood yet.

This work designed a novel solid solution photocatalyst $Bi_{1-x}Ce_xVO_{4+\delta}$ to further investigate the influence of lanthanide ions on the electron–hole pair separation and the photocatalytic activity. It is a new challenge to compose photocatalytic materials with the structure of solid solution. Within this configuration, the improvement of separation efficiency of photogenerated electron–hole pairs might be reached by creating donor and acceptor defects in crystal lattice. Cerium is one of the most interesting dopants due to its different electronic structure between Ce^{3+} and Ce^{4+}, leading to different chemical state in crystal lattice. Furthermore, Ce^{3+} and Ce^{4+} possess approximately ionic radius with Bi^{3+},[24] which is conductive to the substitution. In this work, the influence of Ce substituted in crystal lattice on crystal phase, optical

properties, photogenerated charges separation, photocurrents and photocatalytic degradation of methylene blue and phenol under visible light irradiation were investigated in detail. Moreover, the proposed mechanism of the enhanced photocatalytic activity was discussed.

Experimental

Synthesis of $BiVO_4$ and $Bi_{1-x}Ce_xVO_{4+\delta}$ photocatalysts

All chemicals used in this work were of analytical reagent grade (Sinopharm Chemical Reagent Co., Ltd., China) and used without further purification. The solutions were prepared using Milli-Q water. $Bi_{1-x}Ce_xVO_{4+\delta}$ photocatalysts were prepared using hydrothermal method as described below. Proportionate amounts of $Bi(NO_3)_3{\cdot}5H_2O$, $Ce(NO_3)_3{\cdot}6H_2O$ and NH_4VO_3 were weighted according to the stoichiometric formulation $Bi_{1-x}Ce_xVO_{4+\delta}$ (x = 0, 0.005, 0.02, 0.05, 0.1, 0.2, 0.3) (abbreviated as BCVO x below). Subsequently, $Bi(NO_3)_3{\cdot}5H_2O$ and $Ce(NO_3)_3{\cdot}6H_2O$ were mixed and dissolved in 50 mL Milli-Q water and 3 mL nitric acid to form a transparent solution. NH_4VO_3 was dissolved in 50 mL Milli-Q water at 70 °C. Afterwards, Bi^{3+} and Ce^{3+} was added dropwise into NH_4VO_3 solution and NaOH (0.1 M) was injected constantly to ensure the pH value of the system to be *ca.* 10. When the two solutions were entirely mixed, 2 mL H_2O_2 was added. The dark orange slurry was stirred for 15 min followed by being transferred into Teflon-lined stainless steel autoclaves. The sealed reactors were then heated at 180 °C for 24 h. The precipitate was subsequently filtered and washed with Milli-Q water several times to ensure that the residual impurities were removed, and then was dried at 80 °C for 6 h.

Characterization

The crystalline phases of $BiVO_4$ (x=0) and $Bi_{1-x}Ce_xVO_{4+\delta}$ were determined using X-ray diffraction (XRD) (D/MAX-RB, Rigaku, Japan). The diffraction patterns were recorded in the 2θ = 10 to 70° range with a Cu Kα source (λ = 0.15405) running at 40 kV and 30 mA. The specific surface area of samples was determined by Brunauer–Emmett–Teller (BET) method (NOVA 4200e, Quantchrome, USA). The morphology and chemical composition were examined using a scanning electron microscopy (SEM) (S-4800, Hitachi, Japan) equipped with an energy-dispersive X-ray spectrometer (EDS). The high-resolution transmission electron microscopy (HRTEM) images were recorded on a transmission electron microscope (2010F, JEOL, Japan) at

an accelerating voltage of 200 kV. X-ray photoelectron spectroscopy (XPS) was performed on an X-ray photoelectron spectrometer (AXIS ULTRA^{DLD}, Kratos, Japan) using the Al Kα radiation. The Raman spectra at room temperature were obtained with a Raman spectrometer (T64000, Horiba LabRam, France), excited by an Ar^+ laser (530 nm). All measurements were recorded under the same conditions of 2s of integration time and 30 accumulations. The UV–vis diffuse reflectance spectra (DRS) of the photocatalysts were recorded at room temperature using a UV–vis spectrophotometer (T9s, Persee, China) equipped with an integrating sphere. $BaSO_4$ was used as the reference. The photoluminescence (PL) spectra were recorded by a fluorescence spectrophotometer (F-4500, Hitachi, Japan) with a Xe lamp as the excitation light source. The electron paramagnetic resonance (EPR) spectra were performed on an EPR spectrometer (EMX Plus, Bruker, Germany). The spectra were obtained using the microwave power was 20 mW, frequency of 9.85 GHz and 3503 G central magnetic field.

Measurement of photocatalytic activity

The photocatalytic activities of $BiVO_4$ and $Bi_{1-x}Ce_xVO_{4+\delta}$ photocatalysts under visible light were evaluated by degrading 10 mmol/L methylene blue (MB) with an initial absorbance at 664 nm of 1.062 and 40 mmol/L phenol with an initial absorbance at 270 nm of 0.671. A 400 W Xe lamp with an UV-cutoff filter ($\lambda > 420$ nm) was used as a light source and set about 10 cm apart from the reactor. The experiments were performed at 25°C using constant temperature circulating water as follows: 40 mg photocatalyst was dispersed in 40 mL of MB solution and 40 mL phenol solution respectively, followed by stirring for 60 min in the dark to achieve an adsorption–desorption equilibrium before light irradiation. During the irradiation, the reaction samples were collected at 30 min (60 min for phenol degradation) intervals and centrifuged to remove the photocatalyst particles. The ratios (C/C_0) of the MB and phenol concentration were adopted to evaluate the degradation efficiency (i.e., C_0 was the initial concentration, where C was the concentration at certain time) by checking the absorbance spectrum at 664 nm for MB and 270 for phenol using a UV–vis spectrophotometer (U-3900H, Hitachi, Japan).

Photocurrent measurement

The measurement of photocurrent was carried out on an electrochemical

workstation (5060F, RST, China) in a standard three-electrode system with samples, Ag/AgCl electrode (saturated KCl), and a Pt wire used as working electrode, reference electrode, and counter electrode, respectively. And 0.5 mol/L Na_2SO_4 aqueous solution was introduced as electrolyte. A 100 W incandescent lamp with a 420 nm cut off filter was used as the light source. The preparation of working electrode was described below: 5 mg samples were dispersed in 2 mL ethanol and Nafion solution (v/v: 30:1), followed by spread on the bottom middle of ITO glass in a circle with a diameter of 6 mm. Then the photocurrents of the photocatalysts with light on and off were measured at 0.8 V.

Results and Discussion

Structural analysis

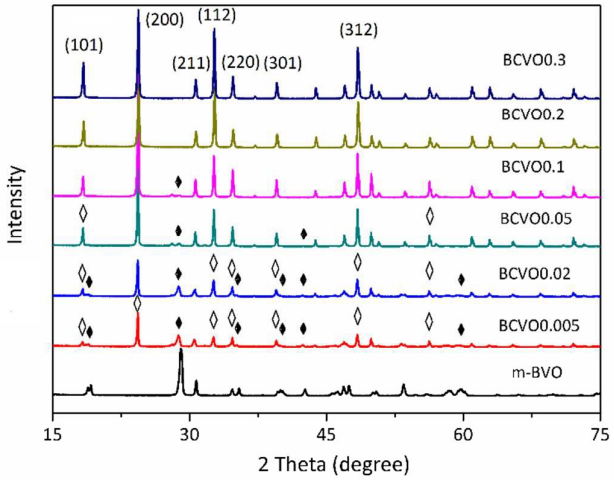

Figure 1. X-ray diffraction patterns for $BiVO_4$ and $Bi_{1-x}Ce_xVO_{4+\delta}$ photocatalysts obtained by hydrothermal synthesis at 180 °C for 24 h: (◆) scheelite-type monoclinic phase; (◇) zircon-type tetragonal phase

Figure 1 presents the X-ray diffraction patterns of the $BiVO_4$ and $Bi_{1-x}Ce_xVO_{4+\delta}$ photocatalysts obtained by hydrothermal synthesis at 180 °C for 24 h. It can be observed that the scheelite-type monoclinic phase was only attained for no Ce-substituted sample (JCPDS card no. 14-0688, abbreviated as m-BVO below). As shown in Figure 1, the low-level substituted photocatalysts were in a mixture phase of monoclinic and tetragonal phase. Even in the sample BCVO 0.005, an obvious trace of phase transition to tetragonal phase could be revealed at 2θ of 18.3°, 24.3°, 32.7° and 48.5° which were respectively indexed as (1 0 1), (2 0 0), (1 1 2) and (3 1 2)

planes of the zircon-type tetragonal $BiVO_4$ (JCPDS card no. 14-0133). As the *x* value increased, the intensity of the tetragonal phase increased whereas the intensity of the monoclinic phase decreased. When *x* was 0.2 and 0.3, the main peaks of the monoclinic phase could hardly be observed and these samples were almost in standardly tetragonal phase. Meanwhile, no signals of Ce_2O_3 and CeO_2 were found even for samples with higher cerium content. Different from the XRD results in our previous work about $CeO_x/BiVO_4$ composites,[19] the monoclinic phase was only attained for $BiVO_4$ sample which means that the cerium ions probably substituted for Bi^{3+} in crystal structure rather than loaded at surface as oxide crystal grains.

Raman spectroscopy can provide more structural information and was used to support the transformation from monoclinic to tetragonal phase as cerium ions ratio increased. The Raman spectra of the $BiVO_4$ and $Bi_{1-x}Ce_xVO_{4+\delta}$ photocatalysts are shown in Figure 2. In the spectra of m-BVO, the strongest mode at 828.4 cm^{-1} is attributed to the symmetric V−O stretching mode ν_s(V−O) and the weak shoulder at near 710.8 cm^{-1} is assigned to the asymmetric V−O stretching mode ν_{as}(V−O) of monoclinic phase. The doublet peaks observed at about 364.8 cm^{-1} and 324.9 cm^{-1} are attributed to the symmetric bending mode $\delta_s(VO_4)$ and the asymmetric bending mode $\delta_{as}(VO_4)$, respectively. The external modes (rotation/translation) are observed at 209.5 cm^{-1} and 124.6 cm^{-1}. However, in the spectra of $Bi_{1-x}Ce_xVO_{4+\delta}$ samples, the strongest mode that assigned to the symmetric V−O stretching mode ν_s(V−O) shifted to 851.9 cm^{-1} and the weak shoulder also had obvious blue shift. An empirical relationship between the Raman shift and the metal–oxygen bond length has been established for vanadium ($\nu = 21349 \times exp\ (-1.9176\ R)$, where ν is the Raman shift in cm^{-1} and *R* is the V−O bond length in Å),[25-27] in which the higher frequencies (blue shift) of the Raman stretching band correspond to the shorter bond length in V−O of tetragonal phase. The Raman spectra of BCVO 0.005 obviously showed the mixture modes of tetragonal phase and monoclinic phase while the ν_s(V−O) mode of monoclinic phase declined as the *x* value increased, which was in accordance with the XRD patterns. Additionally, the disappearance of the bending mode $\delta(VO_4)$ doublet of monoclinic phase and the external modes appear at 248 cm^{-1} were also evidences of this phase transition. Furthermore, Raman spectra can also be a sensitive method to investigate the doping site in the crystal lattice. The translation and rotation modes of 124.6 cm^{-1} and 209.5 cm^{-1} are at a much lower frequency than the internal modes of VO_4, which refer to the motion of the VO_4 as rigid units

and is sensitive to the change of unit mass, because they involve heavier VO_4 units and weaker coupling interactions.[28] It can be seen from Figure. 2 before the disappearance of the external modes that no obvious shift was observed though the mass of Ce is much higher than that of V. This result demonstrated that Ce did not substitute for V in crystal lattice.

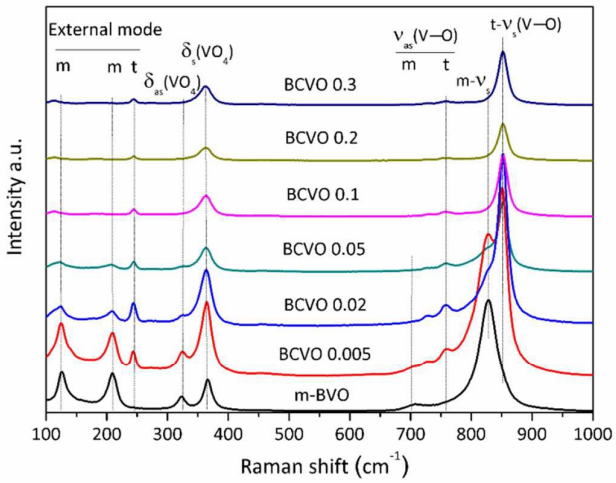

Figure 2. Raman spectra for the $BiVO_4$ and $Bi_{1-x}Ce_xVO_{4+\delta}$ photocatalysts obtained by hydrothermal synthesis at 180 °C for 24 h

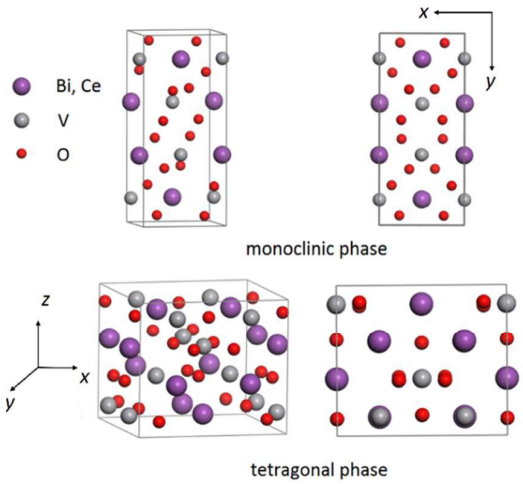

Figure 3. Schematic crystal structures of scheelite-type monoclinic and zircon-type tetragonal phase

At the same time, it is worthy to note that increasing the content level of substituted cerium, a slight decrease in cell parameters and crystal volume, that were refined from the X-ray diffraction data of the $BiVO_4$ and $Bi_{1-x}Ce_xVO_{4+\delta}$ photocatalysts, was observed in Table 1. This phase transition would be achieved by considering the

substitution of cerium ions in Bi^{3+} positions. On this basis, the decrease in the cell parameters and crystal volume was probably attributed to the smaller ionic radius of Ce^{4+} (0.97 Å) and Ce^{3+} (1.143 Å) in comparison to that of Bi^{3+} (1.17 Å) with coordination number of 8.[29] The substitution of cerium ions was also reflected in the decline of the Raman band intensity with the content level increasing, suggesting the weak deformation of VO_4 tetrahedron (Figure 2).[30] Accordingly, the schematic crystal structures of monoclinic and tetragonal phase can be built based on the preceding analysis and the refined XRD data of samples, as it is shown in Figure 3.

Table 1. Surface area, band gap and structural characterization of the $BiVO_4$ and $Bi_{1-x}Ce_xVO_{4+\delta}$ photocatalysts refined from XRD data

Photocatalyst	Surface area (m^2/g)	Band gap (eV)	Crystal Vol ($Å^3$)	Lattice Parameters		
				a (Å)	*b* (Å)	*c* (Å)
m-BVO	33.46	2.46	306.85	5.184	11.659	5.077
BCVO 0.005	17.42	2.76	344.91	7.306	7.306	6.462
BCVO 0.02	23.61	2.74	344.97	7.307	7.307	6.461
BCVO 0.05	28.38	2.66	344.65	7.305	7.305	6.458
BCVO 0.1	33.11	2.80	344.51	7.303	7.303	6.458
BCVO 0.2	42.75	2.81	343.82	7.299	7.299	6.453
BCVO 0.3	11.54	2.84	343.35	7.298	7.298	6.453

Morphology characterization

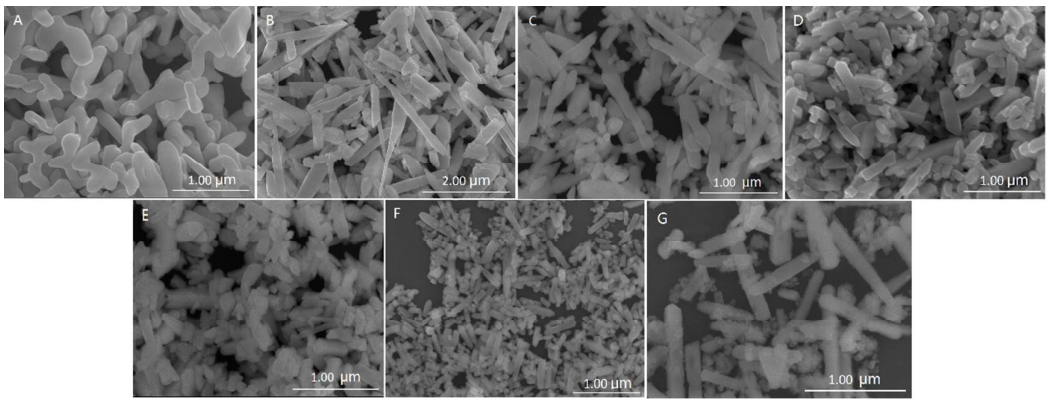

Figure 4. SEM photos of (A) $BiVO_4$, $Bi_{1-x}Ce_xVO_{4+\delta}$ photocatalysts with (B) x = 0.005, (C) x = 0.02, (D) x = 0.05, (E) x = 0.1, (F) x = 0.2, (G) x = 0.3

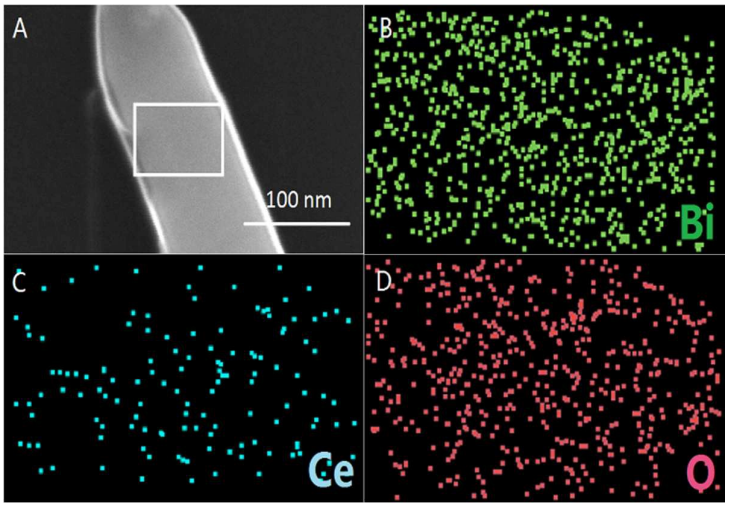

Figure 5. High-magnification of BCVO 0.2 and the element mapping images

The phase transition also had a significant effect on the morphology of as-obtained photocatalysts, as it is shown in Figure 4. The morphology of the $BiVO_4$ (Figure 4(A)) shows buckhorn-like structure as it was in our previous work,[19] and its surface area is 33.46 m^2/g according to Table 1. However, it is clear that $Bi_{1-x}Ce_xVO_{4+\delta}$ photocatalysts in Figure 4(B)-(G) generally showed nanorod morphologies. From the Figure 4(B) of sample BCVO 0.005, it can be seen that the rod size was larger than that of $BiVO_4$. With the increase of cerium content until 20 at.% (x = 0.2), the size of the nanorods decreased gradually and the nanorods became less cluster. Whereas, for the sample with the highest cerium content BCVO 0.3 shown in Figure 4(G), the dispersive and larger rod-like particles with hundreds nanometers width and several micrometers length came into being. Meanwhile, the surface area in Table 1 also confirmed that when the x value was 0.005, 0.02, 0.05, 0.1 and 0.2, the surface area of the samples first decreased to 17.42 m^2/g and then increased as 23.61, 28.38, 33.11 and 42.75 m^2/g, and it decreased again to 11.54 m^2/g when the x is 0.3. This signifies that the presence of cerium in the reaction media may influence the formation of crystalline particles through a characteristic nucleation–dissolution–recrystallization effect in the processing.[31] The substituted Ce induced the crystalline particles to grow into the new morphology and the particle size decreases with the cerium content increasing. However, the larger particle size of high-level cerium contain sample (x=0.3) might be derived from Ostwald Ripening during the process of recrystallization. The homogenous combination of photocatalyst $Bi_{1-x}Ce_xVO_{4+\delta}$ was further confirmed by EDS analysis. Figure 5 illustrates the photo of an individual

BCVO 0.2 nanorod with about 100 nm width and displays the representative element mapping images. Vanadium was also homogeneous and not displayed here. It demonstrates an even distribution of the elements in the frame imaging area, reasonably indicating that cerium dissolved into the substrate evenly.

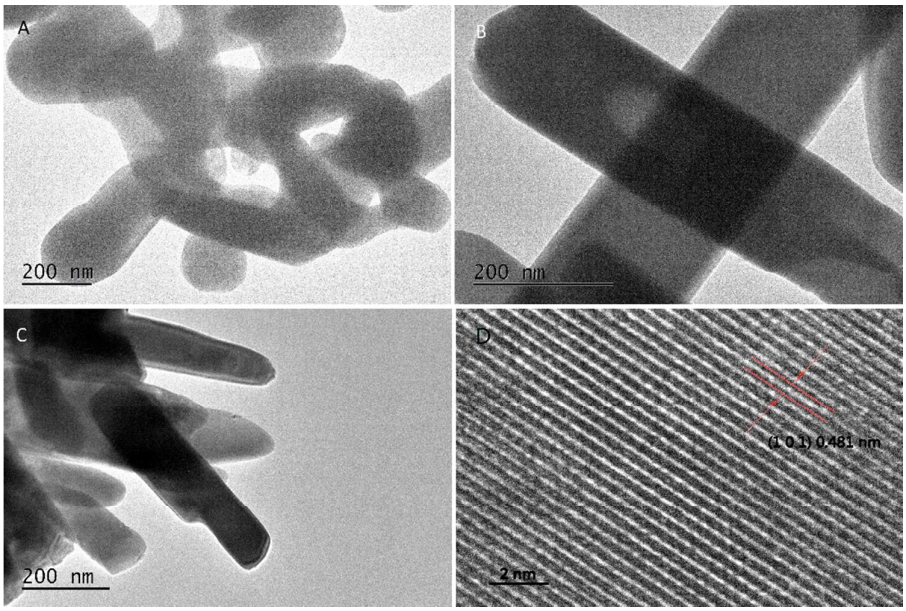

Figure 6. TEM images of (A) $BiVO_4$, $Bi_{1-x}Ce_xVO_4$ photocatalysts with (B) x = 0.1, (C) x = 0.2, and (D) HRTEM image of BCVO 0.2

The high-resolution transmission electron microscopy is widely used to characterize the microstructure of nanomaterials. Figure 6 shows the TEM and HRTEM images of $BiVO_4$, BCVO 0.1 and BCVO 0.2 photocatalysts. The TEM images (Figure 6(A)-(C)) clearly confirms that the $BiVO_4$, as well as Ce-contained samples, had smooth surface and edged shape, which implied that cerium species almost anchored into the crystal lattice. As it is shown in Figure 6(D), the distinct lattice fringes reveal that the BCVO 0.2 nanorod was well crystallized. The lattice spacing of 0.481 nm in Figure 6(D) corresponded to the (1 0 1) crystalline plane of tetragonal phase according to JCPDS card no. 14-0133, whereas lots of defective dots can be observed along the lattice fringes, which reasonably indicated that substitution of cerium ions in Bi^{3+} positions could lead to the formation of some lattice defects.

Chemical state analysis

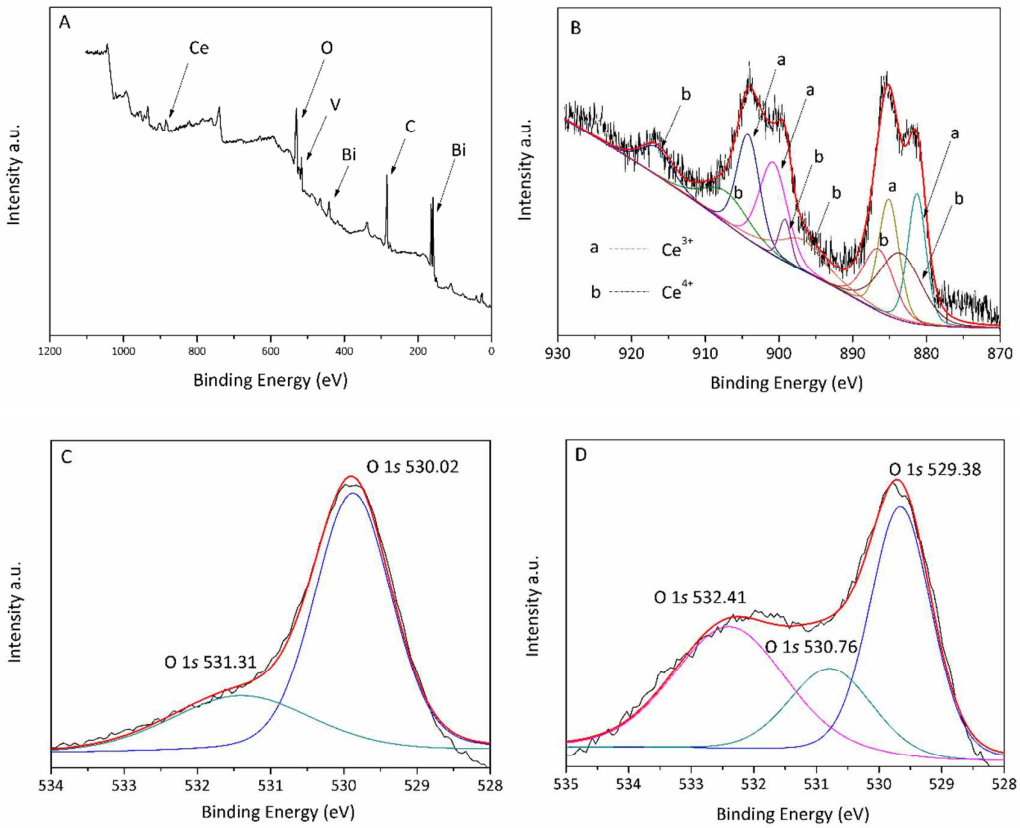

Figure 7. XPS analysis of (A) overall XPS spectra, (B) Ce 3*d* peaks and (D) O 1*s* peaks of BCVO 0.2 photocatalyst; (C) O 1*s* peaks of $BiVO_4$ photocatalyst

The chemical state of solid solution photocatalysts, especially the effects of unequal-valence substitution on the chemical state, which probably could significantly influence the photocatalytic performance, were further revealed using XPS analysis. The shift of peaks position was calibrated using the binding energy of C 1*s* at 284.8 eV before analysis. Figure 7(A) shows the overall XPS spectra of BCVO 0.2, and only the characteristic peaks of Bi, Ce, V and O were detected. Moreover, the observed peak of C 1*s* was attributed to the signal from carbon in the instrument. No XPS characteristic peaks of N 1*s* was detected at around 400 eV although the raw material ammonium metavanadate contained nitrogen element, which indicated no nitrogen doped in as-prepared photocatalysts. There was no significant change in the peaks position of Bi^{3+} ions and V^{5+} ions after substitution, which were not displayed here. The XPS peaks of the Ce 3*d* are well known to be complicated because of the hybridization of Ce 4*f* orbital with ligand orbital and fractional occupancy of the valence 4*f* orbital.[32] Figure 7(B) illustrates that the Ce 3*d* spectra were composed of

three doublet peaks in the case of Ce^{4+} species and two doublet peaks in the case of Ce^{3+} species. The peaks *a* locating at about 881.27 and 885.11 eV in the low binding energy region and at about 899.21 and 904.24 eV in the high binding energy region were respectively assigned to Ce $3d_{5/2}$ and Ce $3d_{3/2}$. These states corresponded to the final states of $3d^9 4f^1$ and $3d^9 4f^2$ considering the spin–orbit splitting, which indicated the presence of Ce^{3+} in crystal lattice.[33] The peaks *b* in Figure 7(B) at the binding energy of 883.54, 886.49, and 897.78 eV and their spin–orbit splitting peaks at 900.78, 907.02, and 916.59 eV were attributed to Ce $3d_{5/2}$ and Ce $3d_{3/2}$ of Ce^{4+} as a result of the $3d^9 4f^1$, $3d^9 4f^2$, and $3d^9 4f^0$ final states.[34] Accordingly, from the above results it is quite clear that there is coexistence of Ce^{3+} and Ce^{4+} in the crystal lattice of the solid solution photocatalysts. Figure 7(C) shows the XPS peak of O 1*s* level in the $BiVO_4$, which located at 530.02 eV corresponding to the O^{2-} in crystal lattice. The weak peak for O 1*s* locating at about 531.31 eV was attributed to the O–H bonds of absorbed water on the sample surface.[35] There is no other peaks in the O 1*s* XPS spectra of the $BiVO_4$ because the binding energy of metal–oxygen bond almost locate at around 530 eV.[36,37] However, the O 1*s* XPS peak of BCVO 0.2 for O^{2-} species is much more different after Ce substitution, as it is shown in Figure 7(D). Three peaks were obtained after the Gausssian-Lorentzian fitting for the O 1*s* XPS spectra of BCVO 0.2. One of these peaks locating at the binding energy of 529.38 eV was assigned to the O–Bi bonds in crystal lattice. It needs to be noticed that this peak shifted to the low binding energy region by about 0.7 eV in comparison to that of the $BiVO_4$, which was attributable to the formation of Ce–O–Bi bonds as a result of the substitution of Ce ions at Bi^{3+} positions.[38,39] The small peak at 530.76 eV was also attributed to the O–H bonds at the surface of photocatalyst. And most obviously, a new peak at about 532.41 eV was observed in the spectra for O 1*s* after Ce substitution. This peak was most probably corresponded to the nonstoichiometric O species and interstitial O_2^{2-} in the solid solution crystal lattice.[40,41]

Optical properties

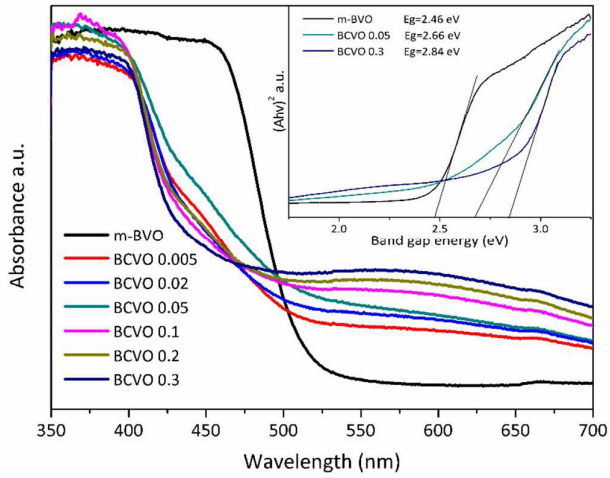

Figure 8. The UV-vis diffuse reflectance spectra of the $BiVO_4$ and $Bi_{1-x}Ce_xVO_{4+\delta}$ photocatalysts; the inset shows the band gap energy of the m-BVO, BCVO 0.05 and BCVO 0.3

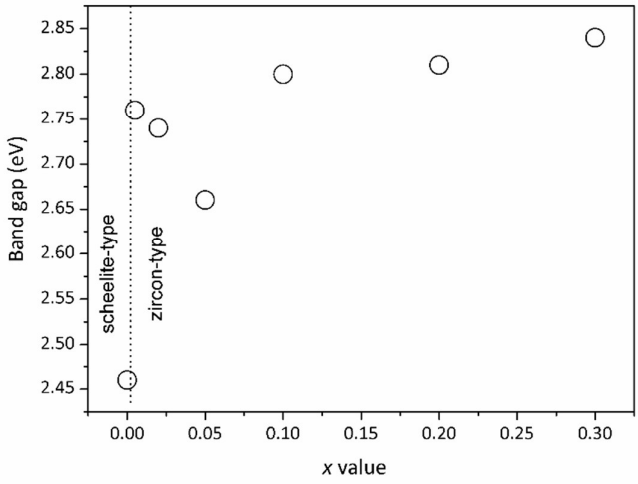

Figure 9. Band gap energy variation as a function of x in $Bi_{1-x}Ce_xVO_{4+\delta}$ photocatalysts

The UV–vis diffuse reflectance spectra of $Bi_{1-x}Ce_xVO_{4+\delta}$ photocatalysts in comparison with $BiVO_4$ are shown in Figure 8. It is clear that the progressive appearance of the tetragonal phase also had a significant effect on the absorption edges of the photocatalysts. As it is shown in Figure 8, the m-BVO presented an absorption band within the visible range while the Ce-substituted samples showed an absorption band just in the transitional region between UV and visible range. The newly appeared absorption by Ce-substituted photocatalysts in the region of $\lambda > 500$ nm may be introduced by *f-f* transition of cerium species[20] and the absorption improved with the increasing of Ce concentration, which illustrated the Ce ions in crystal lattice could arouse a significant effect on the optical properties of $BiVO_4$. The

optical band gap for the semiconductor photocatalysts was estimated using the following equation:

$$(Ahv) = a(hv - E_g)^{n/2}$$

where *A* was the absorption coefficient near the absorption edge; *h* was the Planck constant with the unit of eV; *a* was a constant; E_g was the absorption band gap energy; $BiVO_4$ had a direct band gap, and *n* was 1 herein.[11] The inset of Figure 8 shows curves of $(Ahv)^2$ plots versus photon energy (*hv*) of m-BVO, BCVO 0.05 and BCVO 0.3 photocatalysts. The band gap of BCVO 0.05 and BCVO 0.3 were estimated to be about 2.66 and 2.84 eV, respectively, which implied that the adsorption edges of solid solution samples shifted towards UV region in comparison to that of m-BVO (2.46 eV). The band gap of the whole $Bi_{1-x}Ce_xVO_{4+\delta}$ ($0 \leq x \leq 0.3$) system as a function of x value was taken into account and showed in Figure 9. The crystalline structure changed from scheelite-type to zircon-type when cerium was introduced, so the band gap variation with composition must be discussed separately according to Vegard's law.[42] The band gap of BCVO 0.005 was 2.76 eV and first sharply decreased to about 2.66 eV at x = 0.05, and then increased non-linearly to 2.84 eV with the increasing of x value. Apparently, this result was accordance with the so-called bowing effect as reported by Zhou *et al*.[43] However, the situation here was more complex because of the re-transformation of crystalline structure at $x > 0.6$.[44] Hence, no further comment and bowing fitted was made on this issue. Anyway, the band structure of $BiVO_4$ changed as the phase transition as well as the composition variation, and the band gap of all the investigated samples were listed in Table 1.

Photocatalytic properties

The photocatalytic performance of the prepared $BiVO_4$ and $Bi_{1-x}Ce_xVO_{4+\delta}$ samples was first evaluated by examining the photodegradation of MB under visible-light irradiation, as shown in Figure 10.

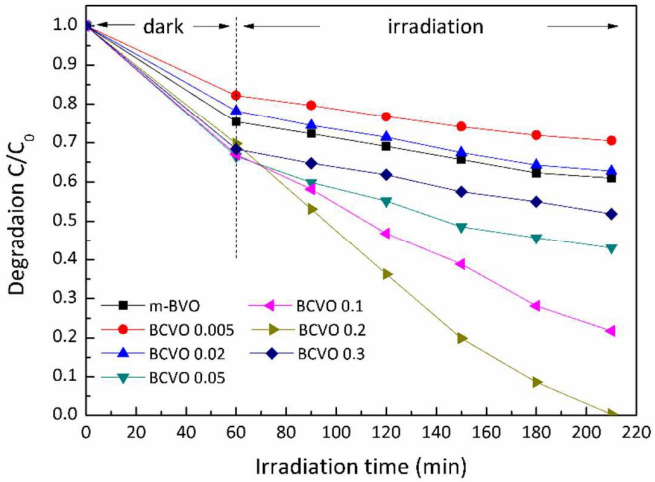

Figure 10. Comparison of the adsorption in dark and degradation ratio of MB using $BiVO_4$ and $Bi_{1-x}Ce_xVO_{4+\delta}$ samples under visible-light irradiation

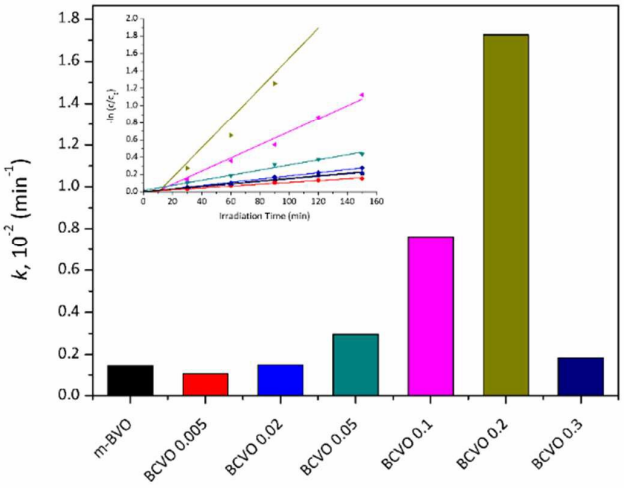

Figure 11. Kinetic constants of the MB decomposition over different samples

All samples were dispersed in MB solution followed by stirring for 60 min in the dark to achieve an adsorption–desorption equilibrium before light irradiation. Figure 10 shows that the photodegradation rate of MB for the m-BVO, BCVO 0.1 and BCVO 0.02 was about 39%, 36% and 31% respectively after 150 min of irradiation, which indicated that only a little part of MB was degraded by m-BVO and the low content Ce-contained photocatalysts. This implied that a small amount of cerium substitution probably formed the recombination center for the photogenerated charges because of the short-circuiting mechanism, resulting in reducing the activity of photocatalysts. As shown in Figure 10, it is clear that with the subsequently increase of cerium content, the photocatalytic activity of Ce-contained samples enhanced obviously. The

degradation ratios of MB using BCVO 0.05 and BCVO 0.1 were raised to about 64% and 78% respectively after 150 min of irradiation. Especially when the cerium content was 20 at.% (BCVO 0.2), a sharp decrease of MB concentration was observed, and the MB could be entirely degraded within 2 hours under visible-light irradiation. However, the content of cerium sequentially increasing to 30 at.% (BCVO 0.3) would lead to the decrease of its photocatalytic performance. A pseudo-first-order kinetic model was used to fit the degradation data. Figure 11 illustrates the apparent kinetic rate constants of the MB decomposition over different samples. The rate constant (k) was calculated to be 1.726×10^{-2} min^{-1} for the BCVO 0.2, approximately ten-times enhancement in comparison to that of m-BVO. Generally, the bigger surface area will provide more active reaction site for both adsorption and degradation. It needs to be noticed that BCVO 0.05, BCVO 0.1 and BCVO 0.2 showed much higher photocatalytic activity than that of m-BVO, though they hold approximate specific surface area according to Table 1. These findings clearly demonstrated that the enhanced photocatalytic activity was not mainly derived from the variation of the surface area.

In addition to MB, a typical colorless contaminant, phenol, was also chosen to further evaluate the photocatalytic performance of the samples. There was nearly no adsorption of phenol after 60 min stirring in the dark and the photodegradation rate of phenol for m-BVO and BCVO 0.2 were recorded in the Figure 12.

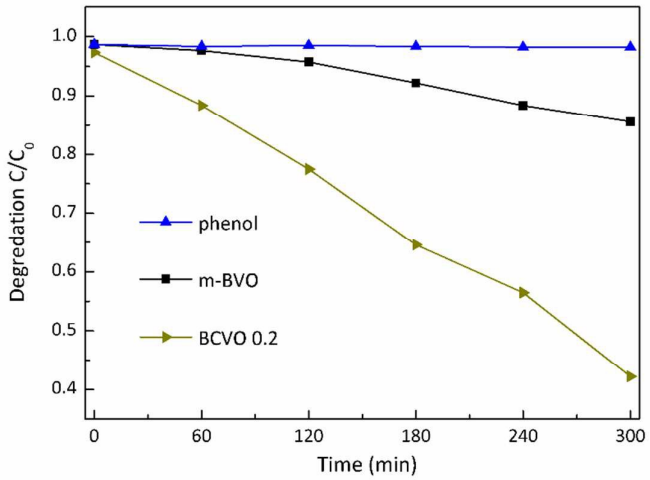

Figure 12. Degradation ratio of phenol using m-BVO and BCVO 0.2 under visible-light irradiation

The results indicated that phenol could hardly degrade under visible-light irradiation without photocatalyst and about 58.6% of phenol was degraded using BCVO 0.2. However, only about 13.4% of phenol could be degraded using m-BVO at the

constant experimental conditions. The photocatalytic degradation rate of the phenol for BCVO 0.2 is more than four times higher than that of pure $BiVO_4$. Figure 13 (A) and (B) shows the temporal absorption spectral changes of phenol in photodegradation over m-BVO and BCVO 0.2 under visible-light irradiation. Although an obvious absorption peak at 270 nm could be observed after irradiation for 300 min, the absorption peak at 270 nm was much declined for BCVO 0.2 as shown in Figure 13 (B), compared to the m-BVO. These findings further confirmed the enhanced photocatalytic activity of the appropriate Ce-contained solid solution photocatalyst.

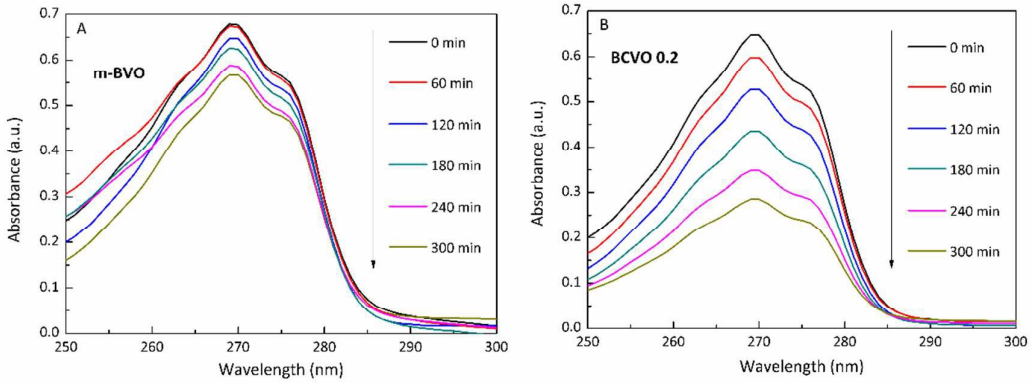

Figure 13. Time-dependent UV–vis absorption spectra of the phenol in the presence of various photocatalysts: (A) m-BVO and (B) BCVO 0.2

Mechanism of improved photocatalytic activity

Lower photoactivities reported in the literature for tetragonal phase $BiVO_4$ were explained considering the wider band gap for this phase.[5,6] Whereas in our case, the solid solution with relative wide band gap showed outstanding photocatalytic performance. A possible mechanism can be proposed to illustrate the reasons of the high photocatalytic activity of the solid solution photocatalysts compared to $BiVO_4$ through the following defect reactions written in the Kroger–Vink notation (equation (1, 2, 3)) based on the preceding analysis:

For Ce^{3+}

$$\mathrm{CeV}O_4 \xrightarrow{BiVO_4} Ce_{Bi} + V_V + 4O_O \quad (1)$$

For Ce^{4+}

$$Ce_3(VO_4)_4 \xrightarrow{3BiVO_4} 3Ce_{Bi}^{\cdot} + 3V_V + V_i^{5\cdot} + 12O_O + 4O_i'' \quad (2)$$

$$Ce_3(VO_4)_4 \xrightarrow{4BiVO_4} 3Ce_{Bi}^{\cdot} + Va_{Bi}''' + 4V_V + 16O_O \quad (3)$$

As shown in equation (1), Ce^{3+} may occupy Bi^{3+} positions with the substitution of equal electrical charge. In principle, no charged defect creates in this case. Whereas, there are number of possible charged defect states, $Ce_{Bi}^{\cdot}$, Va_{Bi}''', $V_i^{5\cdot}$ and O_i'', in the substituted crystal lattice, which Ce^{4+} ions can introduced according to the equation (2) and (3). The interstitial O_i'' in the crystal structure of $Bi_{1-x}Ce_xVO_{4+\delta}$ may be existence as O_2^{2-} species, which was demonstrated by the newly creating XPS peak for O 1*s* after substitution (Figure 7(D)).

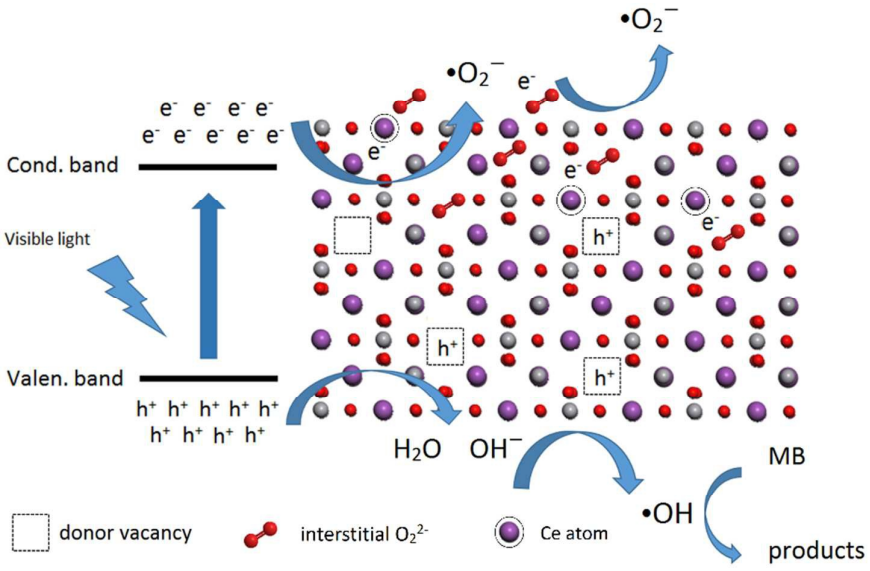

Figure 14. Schematic possible mechanism for the separation of photogenerated electron–hole pairs and the production of $\bullet O_2^-$ and •OH

It is commonly accepted that the performance of photodegradation in the heterogeneous photocatalytic system come from the strong oxidizing property of active species hydroxyl radicals (•OH) and superoxide anion radicals ($\bullet O_2^-$) generated under irradiation. Figure 14 illustrates the possible mechanism for the enhanced separation efficiency of photogenerated electron–hole pairs and the degradation of MB under visible light irradiation. As shown in the schematic, photo-excited electrons (e^-) were generated from the valence band into the conduction band of $Bi_{1-x}Ce_xVO_{4+\delta}$ when the samples were irradiated under visible light. Meanwhile, the corresponding holes (h^+) were leaving in the valence band. In the process of transferring to the photocatalysts surface, the photo-excited electrons (e^-) were

trapped by the acceptor defects ($Ce_{Bi}^{\cdot}, V_i^{5\cdot}$) and the holes ($h^+$) were trapped by the donor defects (Va_{Bi}''',O_i''), which efficiently depress the recombination of electron–hole pairs. However, excess charged defects in crystal lattice could form associated center under Coulomb interaction, which made only a few electron or hole can transfer to the surface of catalyst, resulting in the decline of photocatalytic activity (the photocatalytic activity of BCVO 0.3 in Figure 10, 11). The holes (h^+) transferred to the surface could oxidize the H_2O and OH^- to hydroxyl radicals (•OH) which played an important role in the photocatalytic oxidation process. Another important active species, superoxide anion radicals ($\bullet O_2^-$), were produced by excited electrons (e^-) reduced interstitial O_2^{2-} species and adsorbed O_2. In the end, MB can be oxidized and degraded by these active species. The main reactions were concluded as follows:

$$semiconductor \xrightarrow{hv} e_{CB}^- + h_{VB}^+$$

$$OH^- + h_{VB}^+ \rightarrow \bullet OH$$

$$O_2(O_2^{2-}) + e_{CB}^- \rightarrow \bullet O_2^- + (2e^-)$$

$$\bullet O_2^- + H^+ \rightarrow \bullet O_2H$$

$$\bullet OH + \bullet OH \rightarrow H_2O_2$$

$$H_2O_2 + \bullet O_2H \rightarrow \bullet OH + H_2O + O_2$$

$$MB + \bullet OH \rightarrow product$$

The effective separation of photogenerated electron–hole pairs was confirmed by PL analysis. Figure 15 shows the photoluminescence spectra of the $BiVO_4$ and $Bi_{1-x}Ce_xVO_{4+\delta}$ samples. The luminescence signal at around 600 nm is actually a character PL peak of $BiVO_4$, which corresponded to the recombination of the hole (h^+) formed in the O 2*p* and the electron (e^-) in the V 3*d*.[45] It implied that the lower peak corresponded to the more effective separation of electron-hole pairs. As shown in Figure 15, obvious decreases in PL intensities were observed for the $Bi_{1-x}Ce_xVO_{4+\delta}$ samples with the *x* value higher than 0.005. When *x* is 0.2, the PL peak was much more declined in comparison to that of m-BVO and BCVO 0.005. These findings reasonably indicated that the appropriate presence of the charged defects in solid solution crystal lattice could effectively suppress the recombination of photogenerated electron-holes pairs.

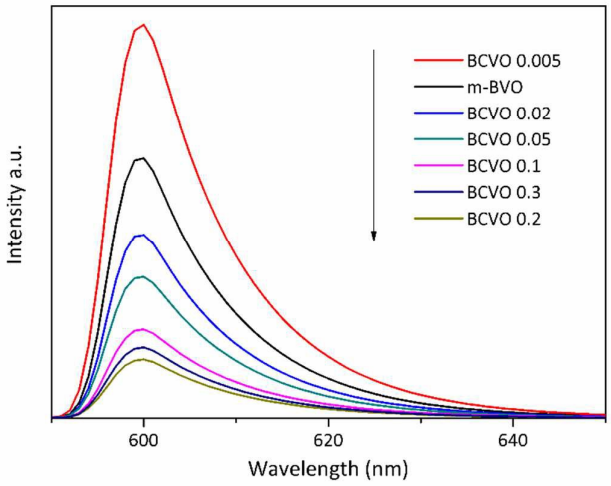

Figure 15. The photoluminescence spectra of the $BiVO_4$ and solid solution samples

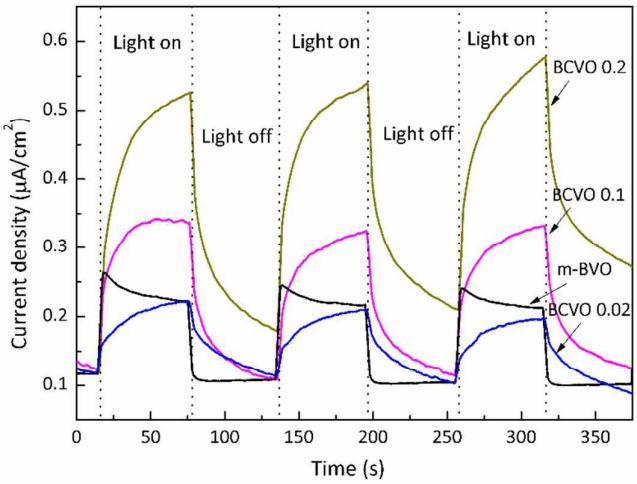

Figure 16. Photocurrent responses of m-BVO, BCVO 0.02, BCVO 0.1 and BCVO 0.2 under the visible light irradiation

The photocurrent responses of photocatalysts in an electrolyte under visible light directly correlate with the generation and transfer of the photoinduced charge carriers in the photocatalytic process, which can further confirm the separation of electron-holes pairs.[46] Figure 16 shows the photocurrent responses of m-BVO, BCVO 0.02, BCVO 0.1 and BCVO 0.2 with light on and off. It is clear that the photocurrent responses of BCVO 0.1 and BCVO 0.2 were much higher than that of m-BVO and BCVO 0.02. Compared with the pure $BiVO_4$, BCVO 0.2 exhibited the most enhanced photocurrent response. It implied that a more efficient separation of photogenerated electron–hole pairs and fast transfer of photoinduced charge carriers occurred in BCVO 0.2 sample. Additionally, it needs to be noticed that all the Ce-contained

samples hold residual current with light off. This probably attributed to the lattice defects in solid solutions, which could release the trapped electron or hole under thermal motion.[47] Meanwhile, the photocurrent responses of the samples well corresponded to their photocatalytic performance. This reasonably indicated that $Bi_{1-x}Ce_xVO_{4+\delta}$ photocatalysts exhibited much higher utilization efficiency of visible light, though they absorbed less visible light in comparison to the m-BVO according to Figure 8.

To further clarify the reasons of the high photocatalytic activity, the involved active radical species was detected by Spin-trapping electron paramagnetic resonance technique. And DMPO was used to trap the active species produced in the photocatalytic reaction under visible light irradiation. The results are shown in Figure 17 and there was no signal when all the suspensions were in dark. In contrast, four characteristic peaks with intensity of 1:2:2:1 for DMPO-trapped •OH were observed in m-BVO and solid solution samples as shown in Figure 17(A). The signal intensity of DMPO−•OH species produced by m-BVO is so weak, suggesting the limited photoactivity of m-BVO. However, the signal intensity of DMPO−•OH species produced by BCVO 0.1 and BCVO 0.2 increased progressively, corresponding to the enhanced photocatalytic performance as confirmed by the degradation of MB and phenol.

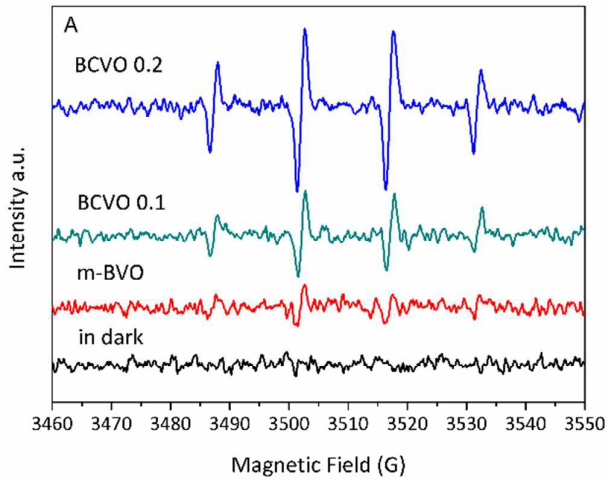

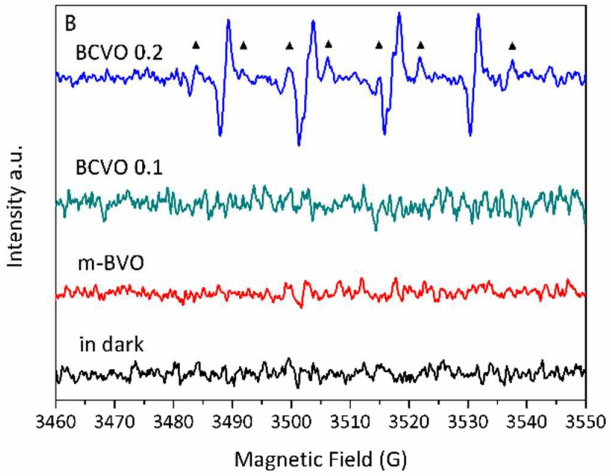

Figure 17. Electron paramagnetic resonance spectra of radical adducts trapped by DMPO in as-prepared photocatalysts dispersion: (A) DMPO−•OH formed and (B) DMPO−• O_2^- (DMPO−methyl radical were marked with ▲) in dark and under irradiation (λ> 420 nm)

DMSO was introduced to quench the signal of DMPO−•OH species in order to detect the EPR signal of DMPO−•O_2^- adducts produced by samples. It can be deduced from Figure 17(B) that only BCVO 0.2 could generate •O_2^- active species in the dispersion. In addition, methyl radical signals derived from •OH radical reactions with DMSO were also observed, which is in accordance with the reported works.[48,49] Generally, •O_2^- is the reduction of absorbed O_2 on catalyst surface and the interstitial O_2^{2-} species in lattice, as illustrated in Figure 14. However, there was no obvious signal of DMPO−•O_2^- produced by m-BVO and BCVO 0.1, though they both creating •OH species. It indicated that the valence band of BCVO 0.2 raised higher than $E_{(O2/O2-\bullet)}$[19,44] after the appropriate substitution of Ce.

To the best of our knowledge, this work may be a first attempt to compose $Bi_{1-x}Ce_xVO_{4+\delta}$ to improve the photocatalytic activity of $BiVO_4$. Although the specific process for the formation of active species was poorly elucidated, there was much reason to believe that the amount of these active species is closely dependent on the separation of photo-excited electron-hole pairs. And it paves the road for the mechanism investigations of the behind.

Conclusion

In summary, monoclinic phase $BiVO_4$ and tetragonal phase $Bi_{1-x}Ce_xVO_{4+\delta}$ photocatalysts have been successfully prepared by homogeneous precipitation with

a hydrothermal method. The studies revealed that the introduction of cerium into $BiVO_4$ lattice brought an obvious change in crystal phase and optical properties. The mole ratio of Bi to Ce in $Bi_{1-x}Ce_xVO_{4+\delta}$ was found to affect the photodegradation of MB and phenol. And the optimum mole ratio was found to be 20% ($Bi_{0.8}Ce_{0.2}VO_{4+\delta}$), showing the best photocatalytic performance under visible-light illumination. The PL spectra and the photocurrent responses indicated the lattice defects in $Bi_{1-x}Ce_xVO_{4+\delta}$ photocatalysts greatly depressed the recombination of electron–hole pairs. Moreover, both •OH and $\bullet O_2^-$ were detected using EPR and the possible mechanism for enhanced photocatalytic activity was proposed. Further detailed studies to fully understand the explicit mechanism about improving the photocatalytic performance under visible light are ongoing in our laboratory.

Acknowledgments

We gratefully acknowledge the financial support provided by the Project of the National Natural Science Foundation of China (Grant No. 21271022).

References

1 H. Fan, T. Jiang, H. Li, D. Wang, L. Wang, J. Zhai, D. He, P. Wang and T. Xie, *J. Phys. Chem. C*, 2012, **116**, 2425–2430.

2 Y. Zhang, G. Li, X. Yang, H. Yang, Z. Lu and R. Chen, *J. Alloys Compd.*, 2013, **551**, 544–550.

3 A. Kudo, K. Omori and H. Kato, *J. Am. Chem. Soc.*, 1999, **121**, 11459–11467.

4 G. Li, D. Zhang and J. Yu, *Chem. Mater.*, 2008, **20**, 3983–3992.

5 S. Tokunaga, H. Kato and A. Kudo, *Chem. Mater.*, 2001, **12**, 4624–4628.

6 G. Tan, L. Zhang, H. Ren, S. Wei, J. Huang and A. Xia, *ACS Appl. Mater. Inter.*, 2013, **5**, 5186–5193.

7 L. Ren, L. Ma, L. Jin, J. Wang, M. Qiu and Y. Yu, *Nanotechnology.*, 2009, **20**, 405602–405610.

8 L. Zhang, D. Chen and X. Jiao, *J. Phys. Chem. B*, 2006, **110**, 2668–2673.

9 G. Liu, S. Liu, Q. Lu, H. Sun, F. Xu and G. Zhao, *J. Sol-Gel Sci. Techn.*, 2014, **70**, 24–32.

10 M. Shang, W. Wang, J. Ren, S. Sun and L. Zhang, *CrystEngComm.*, 2010, **12**, 1754–1758.

11 Y. Hu, D. Li, Y. Zheng, W. Chen, Y. He, Y. Shao, X. Fu and G. Xiao, *Appl. Catal. B: Environ.,* 2011, **104**, 30–36.

12 H. Xu, H. Li, C. Wu, J. Chu, Y. Yan, H. Shu and Z. Gu, *J. Hazard. Mater.*, 2008, **153**, 877–884.

13 M. Guan, D. Ma, S. Hu, Y. Chen and S. Huang, *Inorg. Chem.*, 2011, **50**, 800-805.

14 S. Kohtani, M. Tomohiro, K. Tokumura and R. Nakagaki, *Appl. Catal. B: Environ.*, 2005, **58**, 265–272.

15 L. Ge, *Mater. Lett.*, 2008, **62**, 926–928.

16 F. Lin, D. Wang, Z. Jiang, Y. Ma, J. Li, R. Li and C. Li, *Energy Environ. Sci.*, 2012, **5**, 6400-6406.

17 W. Yao, H. Iwai and J. Ye, *Dalton Trans.*, 2008, **11**, 1426–1430.

18 H. Park, K. Kweon, H. Ye, E. Paek, G. Hwang and A. Bard, *J. Phys. Chem. C*, 2011, **115**, 17870–17879.

19 S. Gu, W. Li, F. Wang, S. Wang, H. Zhou and H. Li, *Appl. Catal. B: Environ.*, 2015, **170**, 186–194.

20 A. Zhang and J. Zhang, *J. Hazard. Mate.*, 2010, **173**, 265–272.

21 H. Xu, C. Wu, H. Li, J. Chu, G. Sun, Y. Xu and Y. Yan, *Appl. Surf. Sci.*, 2009, **256**, 597–602.

22 S. Obregón, S. Lee and G. Colón, *Dalton Trans.*, 2014, **43**, 311–316.

23 J. Huang, G. Tan, L. Zhang, H. Ren, A. Xia and C. Zhao, *Mater. Lett.*, 2014, **133**, 20–23.

24 D. Zhou, L. Pang, J. Guo, Z. Qi, T. Shao, Q. Wang, H. Xie, X. Yao and C. Randall, *Inorg. Chem.*, 2014, **53**, 1048–1055.

25 F. Hardcastle and I. Wachs, *Phys. Chem.*, 1991, **95**, 5031–5041.

26 A. Zhang and J. Zhang, *Mater. Lett.*, 2009, **63**, 1939–1942

27 J. Yu and A. Kudo, *Adv. Funct. Mater.*, 2006, **16**, 2163–2169.

28 W. Luo, J. Wang, X. Zhao, Z. Zhao, Z. Li and Z. Zou, *Phys. Chem. Chem. Phys.*, 2013, **15**, 1006-1013.

29 J. McBride, K. Hass, B. Poindexter and W. Weber, *J. Appl. Phys.*, 1994, **76**, 2435–2441.

30 V. Sadykova, T. Kuznetsova and G. Alikina, *Catal. Today*, 2004, **93–95**, 45–53.

31 S. Obregón and G. Colón, *Appl. Catal. B: Environ.*, 2014, **152–153**, 328–334.

32 H. Borchert, Y. Frolova and V. Kaidiev, *J. Phys. Chem. B*, 2005, **109**, 5728–5738.

33 C. Korsvik, S. Patil, S. Seal and W. Self, *Chem. Commun.*, 2007, **10**, 1056–1058.

34 E. Beche, P. Charvin, D. Perarnau, S. Abanades and G. Flamant, *Surf. Interface Anal.*, 2008, **40**, 264–267.

35 M. Futsuharaa, K. Yoshioka and O. Takai, *Thin Solid Films*, 1998, **317**, 322–325.

36 S. Ho-Kimura, S. Moniz, A. Handoko and J. Tang, *J. Mater. Chem. A*, 2014, **2**, 3948–3953.

37 P. Madhusudan, J. Ran, J. Zhang, J. Yu and G. Liu, *Appl. Catal. B: Environ.*, 2011, **110**, 286–295.

38 A. Dauscher, L. Hilaire, F. Le Normand, W. Müller, G. Maire and A. Vasquez, *Surf. Interface Anal.*, 1990, **16**, 341–346.

39 Y. Luo, G. Tan, G. Dong, H. Ren and A. Xia, *Ceram. Int.*, 2015, **41**, 3259–3268.

40 H. Bosman, A. Pijpers and A. Jaspers, *J. Catal.*, 1996, **161**, 551–559.

41 V. Merupo, S. Velumani, K. Ordon, N. Errien, J. Szade and A. Kassiba, *CrystEngComm*, 2015, **17**, 3366–3375.

42 D. Zhou, L. Pang, H. Wang, J. Guo, X. Yao and C. Randall, *J. Mater. Chem.*, 2011, **21**, 18412-18420.

43 D. Zhou, L. Pang, W. Qu, C. Randall, J. Guo, Z. Qi, T. Shao and Xi Yao, *RSC Advances*, 2013, **3**, 5009-5014.

44 A. Kudo, K. Omori and Hideki Kato, *J. Am. Chem. Soc.*, 1999, **121**, 11459-11467.

45 C. Yu, K. Yang, J. Yu, F. Cao, X. Li and X. Zhou, *J. Alloys Compd.*, 2011, **509**, 4547–4552.

46 Y. Zhang, J. Lu, M. Hoffmann, Q. Wang, Y. Cong, Q. Wang and H. Jin, *RSC Advances*., 2015, **5**, 48983-48991

47 A. Bessiere, S. Sharma, N. Basavaraju, K. Priolkar, L. Binet, B. Viana, A. Bos, T. Maldiney, C. Richard, D. Scherman and D. Gourier, *Chem. Mater.*, 2014, **26**, 1365-1373.

48 P. Vaughan and N. Blough, *Environ. Sci. Technol.*, 1998, **32**, 2947−2953.

49 J. Sun, H. Zhang, L. Guo and L. Zhao, *ACS Appl. Mater. Inter.*, 2013, **5**, 13035−13041.

The recombination of photogenerated charges can be greatly depressed by the charged crystal defects in novel solid solution photocatalyst $Bi_{1-x}Ce_xVO_{4+\delta}$ and both •OH and $•O_2^-$ could be detected in photoreaction.